

Research Article

Inversion Model of GPR Imaging Characteristics of Point Objects and Fracture Detection of Heritage Building

Gao Lv ¹, Ning Li ^{1,2}, Jie Yang^{1,3}, Xianchun Yao ², Dexiu Hu^{1,3} and Rixuan Pang⁴

¹Institute of Water Resources and Hydro-Electric Engineering, Xi'an University of Technology, Xi'an 710048, China

²Institute of Geotechnical Engineering, Xi'an University of Technology, Xi'an 710048, China

³State Key Laboratory Base of Eco-Hydraulic Engineering in Arid Area, Xi'an University of Technology, Xi'an, Shaanxi 710048, China

⁴Geochemical Exploration Team of Shaanxi Geological Mineral Survey Group, Xi'an 710023, China

Correspondence should be addressed to Ning Li; ningli@xaut.edu.cn

Received 29 December 2017; Accepted 20 February 2018; Published 7 May 2018

Academic Editor: Hyung-Sup Jung

Copyright © 2018 Gao Lv et al. This is an open access article distributed under the Creative Commons Attribution License, which permits unrestricted use, distribution, and reproduction in any medium, provided the original work is properly cited.

There are often many hidden structural defects in heritage buildings. As a convenient and effective nondestructive detecting method, ground-penetrating radar (GPR) has a technical advantage in detecting and protecting heritage buildings depending on the advanced image interpretation. The analytic relationship between buried depth and radius of point object and long and short axis of hyperbolic equation was established according to derivations of formulas. The image characteristics of hyperbolic curves with different depth and radius were studied by finite-difference time-domain method (FDTD). And then, inversion models of buried depth and radius of point object were established. The buried depth and radius can be accurately deduced by long and short axis of hyperbolic image. This result was applied in the detection of pedestal defects of the heritage building, and the depth and distribution range of hidden fracture can be accurately interpreted. It provides an effective and fast method to detect hidden defects in civil engineering.

1. Introduction

There have been many point defects in the hidden areas of civil engineering and environmental investigations, such as buried utility mapping, concrete and pavement inspection, and tunnel [1, 2]. Nondestructive testing (NDT) is an effective, flexible, and accurate method for detection of point object. Nowadays, nondestructive techniques which can detect the positions and sizes of point objects are rebound method, ultrasonic method, electrical method, and electromagnetic wave method [3]. Because of high resolution and high flexibility, ground-penetrating radar (GPR) is nowadays considered as one of the most effective and powerful NDT methods [4, 5]. The information of hidden objects, such as the location and geometry, can be deduced by detecting imaging research of point object. It provides a reliable guarantee and basis for the quality inspection and accuracy evaluation.

The detection principle of GPR is as follows. When emitted electromagnetic waves (frequency range is 10–2200 MHz) transmit in the underground, the electromagnetic waves in inhomogeneous relative permittivity of interface will produce the phenomenon of reflection and refraction. And then, the reflected waves, also called echo, can reflect the characteristics of underground medium [6, 7]. However, the relative permittivity of the geological background was complex and unknown in real measurement. This would lead to solution multiplicity in inversion of radius and depth of object [8]. So it is necessary to establish an effective and accurate inversion method.

The most common inversion methods of GPR data are linear inversion (the steepest descent method, the conjugate gradient method, the Gauss-Newton method, the gradient regularization method, etc.) and nonlinear algorithm (simulated annealing algorithm, genetic algorithm, ant colony algorithm, particle swarm optimization, fish

swarm algorithm, etc.) [9, 10]. Because the inversion calculation of nonlinear algorithm needs a lot of time and extensive data, there was less research applied in practical engineering [11, 12]. Linear inversion method exhibits fast convergence speed and excellent numerical stability. But the computed results are multiple local minima points because extremal function tends to be convex.

Herein, a one-to-one relationship between object parameters and inversion parameters was established. We employed a forward modeling method to accurately analyze the relationship between depth and radius of object and long and short axis of hyperbolic imaging. Combined with theoretical derivation and field verification, the imaging features and regularities with different depths and radius were studied. And their multiple regression models with long and short axis of hyperbolic curves were established to achieve the purpose of interpreting the geometry of object. Furthermore, a nondestructive testing of heritage building was carried out to achieve fast interpretation of hidden fracture distribution range and the depth.

2. Mathematical Model of GPR Imaging of Point Object

The antenna of GPR emits electromagnetic waves in the underground. When electromagnetic wave arrives at object, the reflection of signals will occur, and echo signals will be received by receiving antenna [13, 14]. The echo signals contain direct waves, ground reflections, object echoes, and interference signals. Two-dimensional echo data can be obtained by continuous one-dimensional echoes formed by movement of GPR equipment. The scheme is shown in Figure 1. h represents the distance from x to the object. h_0 represents the distance from x_0 to the object. r represents the radius of the object. When geological radar reaches x , the scanning area is a fan-shaped surface. So the object vertically located under x_0 point can be detected. In the time-domain recording, the reflection feature can only be recorded at the x point. And when the GPR reaches x_0 , the detection of the object belongs to the vertical detection.

According to the geometric relationship, we can get the equilibrium

$$(h+r)^2 - (x-x_0)^2 = (h_0+r)^2, \quad (1)$$

$$h = \frac{v \cdot t}{2}, \quad (2)$$

$$h_0 = \frac{v \cdot t_0}{2}, \quad (3)$$

where v is the propagation speed of the electromagnetic wave in the medium. t is the two-way travel time of electromagnetic wave from x to O . t_0 is the two-way travel time of electromagnetic wave from x_0 to O .

Formula (2) is plugged into (1), and the analytic formula of radar imaging of point object is obtained.

$$\left(\frac{t + (2r/v)}{t_0 + (2r/v)} \right)^2 - \left(\frac{x - x_0}{(v/2)t_0 + r} \right)^2 = 1. \quad (4)$$

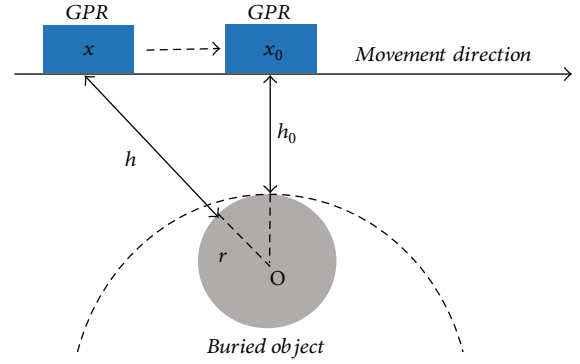


FIGURE 1: Basic principle of point object imaging of GPR.

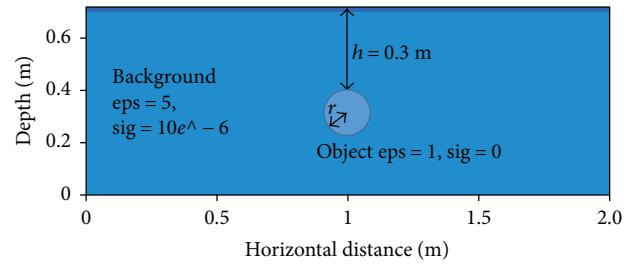


FIGURE 2: Geoelectric model with different radius ($r=0.005$ m, 0.025 m, 0.05 m, and 0.1 m).

Formula (4) conforms to the basic characteristics of hyperbolic equation, and the general formula of hyperbolic equation is as follows:

$$\frac{(y-y_0)^2}{a^2} - \frac{(x-x_0)^2}{b^2} = 1. \quad (5)$$

According to comparative coefficient method, we can get

$$a = t_0 + \frac{2r}{v}, \quad (6)$$

$$b = \frac{v}{2} \left(t_0 + \frac{2r}{v} \right), \quad (7)$$

where a is the long axis of hyperbolic equation. b is the short axis of hyperbolic equation. After transforming (6) and (7), (8) and (9) can be obtained.

$$r = \frac{b(a-t_0)}{a}, \quad (8)$$

$$h_0 = \frac{vt_0}{2} = \frac{bt_0}{a}. \quad (9)$$

Therefore, the characteristics of point object (O) with different depths and radius can be expressed by the long and short axis of the hyperbolic equation. At the same time, the imaging asymptotic lines, eccentricity, and other parameters of the GPR can also be obtained by the ratio of the long axis to short axis.

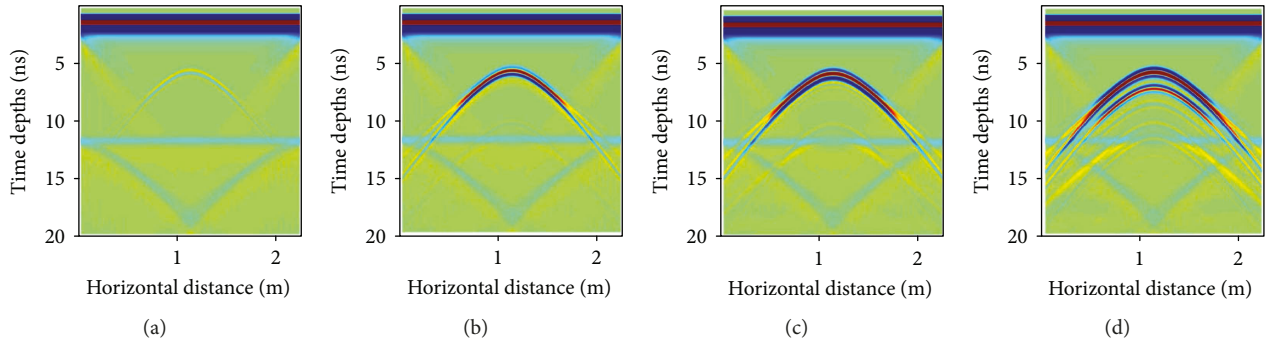


FIGURE 3: (a–d) GPR imaging of different radius ($r = 0.005$ m, 0.025 m, 0.05 m, and 0.1 m).

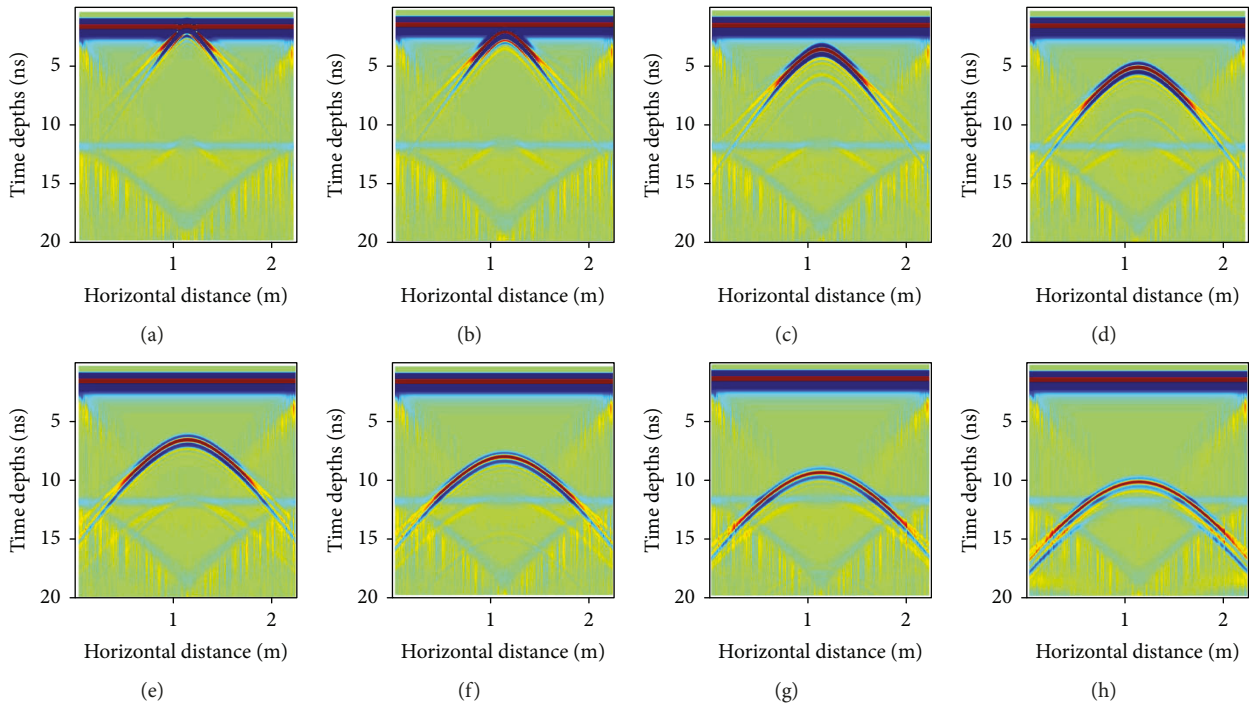


FIGURE 4: (a–h) GPR imaging of different depth ($h = 0.05$ m, 0.10 m, 0.20 m, 0.30 m, 0.40 m, 0.50 m, and 0.60 m).

3. FDTD Forward Modeling of Point Object

In this study, GPR imaging characteristics in different radius and depth of the object were simulated by finite-difference time-domain (FDTD) method, and we employed GprMax software. GprMax [15, 16] is an open source software that simulates electromagnetic wave propagation for the numerical modelling of GPR and has fast computational speed and high computing precision.

3.1. Influence of Different Radius to GPR Imaging. The influence of radius of point object on the GPR imaging is studied by FDTD method. The model design of point object is as follows. The geological background is loess, and the point object is air. The geological model scheme is shown in Figure 2.

The horizontal distance of this model is 2.0 m. The depth of this model is 0.7 m. The cell size is 0.0025 m by

0.0025 m. The time depth is 20 ns. The relative permittivity of geological background is 5. The electrical conductivity of geological background is 0.000001 S/m. The relative permittivity of point object is 1. The electrical conductivity of point object is 0.00 S/m. The depth of point object is 0.4 m. The radius of the point body is 0.005 m, 0.025 m, 0.050 m, and 0.100 m. Dominant frequency is set as 900 MHz. The excitation source is Ricker wavelet. In the numerical simulation, there are 180 step calculations, and each step calculation contains 3391 times. The imaging features of point object with different radius under the same depth are shown in Figure 3.

In Figure 3, the reflectors of point object with different radius appear at about 5 ns. The intensity of the reflected curves is obviously increased, with the increasing of the radius from 0.005 m to 0.100 m. In Figure 4(a), there are only very weak multiple curves. However, there are obviously multiple curves in Figure 4(d). The arc reflected at 5 ns

represents the upper edge of the point object. And the reflection at 6.5 ns represents the lower edge. Moreover, there is no obvious change of opening degree of hyperbola with the increase of the radius of the point object. So the point objects with different radius are not easy to be identified by the opening degree of hyperbola in real detection.

3.2. Influence of Different Depth to GPR Imaging. The influence of depth of point object on the GPR imaging is studied by FDTD method. The depth of object can generally be converted by the time depth and the relative permittivity of the geological background. As the depth of the object changed, the characteristics of radar imaging are bound to be changed. In this section, we established the geological model of objects with different depth, which is as shown in Figure 5.

The basic parameters of this model are as follows. The horizontal distance of this model is 2.0 m. The depth is 0.7 m. The cell size is 0.0025 m by 0.0025. The time depth is 20 ns. The relative permittivity of the geological background is 5, and the conductivity is 0.000001 S/m. The radius of the object is 0.05 m. The relative permittivity of the object is 1. The electrical conductivity of the object is 0 S/m. The depth of the object is set as 5 cm, 10 cm, 20 cm, 30 cm, 40 cm, 50 cm, 60 cm, and 65 cm. The main frequency of wavelet is 900 MHz, and the excitation source is Ricker wavelet. There are a total of 180 calculation steps, and each one is 3392 times. The imaging features of this model are shown in Figure 4.

In Figure 4, the reflection intensity of the hyperbolic image is not obviously changed with the increase of object depth. It demonstrates that reflection intensity is almost not affected by object depth in the same geological background. In addition, the depths of peaks of hyperbolic curves are increasing with the object depths increased. So the key points of hyperbolic curves can be extracted and transformed into time depths to deduce the object depths. Furthermore, opening degree of hyperbola is gradually increased as the object depth increases. According to (8), it can be deduced that object radius is simultaneously determined by propagation time, long axis, and short axis of hyperbolic curves. Therefore, long axis and short axis of hyperbolic curves can be analyzed by opening degree of hyperbola, and then object radius can be deduced.

4. Inversion Model of Geometric Parameters of Object

4.1. Imaging Characteristic Analysis of Objects with Different Radius. The imaging characteristics of point objects are mainly hyperbolic curves. The coordinates of key points of hyperbolic curves can be extracted, and the fitting formulas of hyperbolic curves can be established for regression analysis. In this study, the coordinates of key points were extracted by GetData software (Figure S1). The coordinate values of time depths of different radius were obtained after manual sampling (Table S1). Furthermore, the coordinate values of apparent depths of different radius were obtained

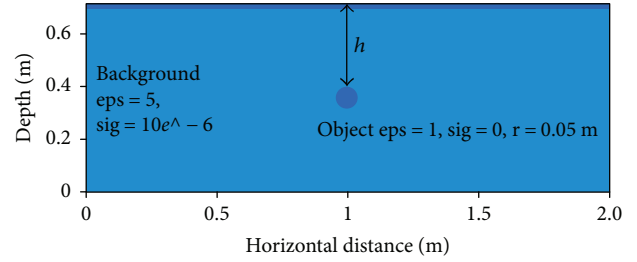


FIGURE 5: Geoelectric model of different depth ($h = 0.05$ m, 0.10 m, 0.20 m, 0.30 m, 0.40 m, 0.50 m, and 0.60 m).

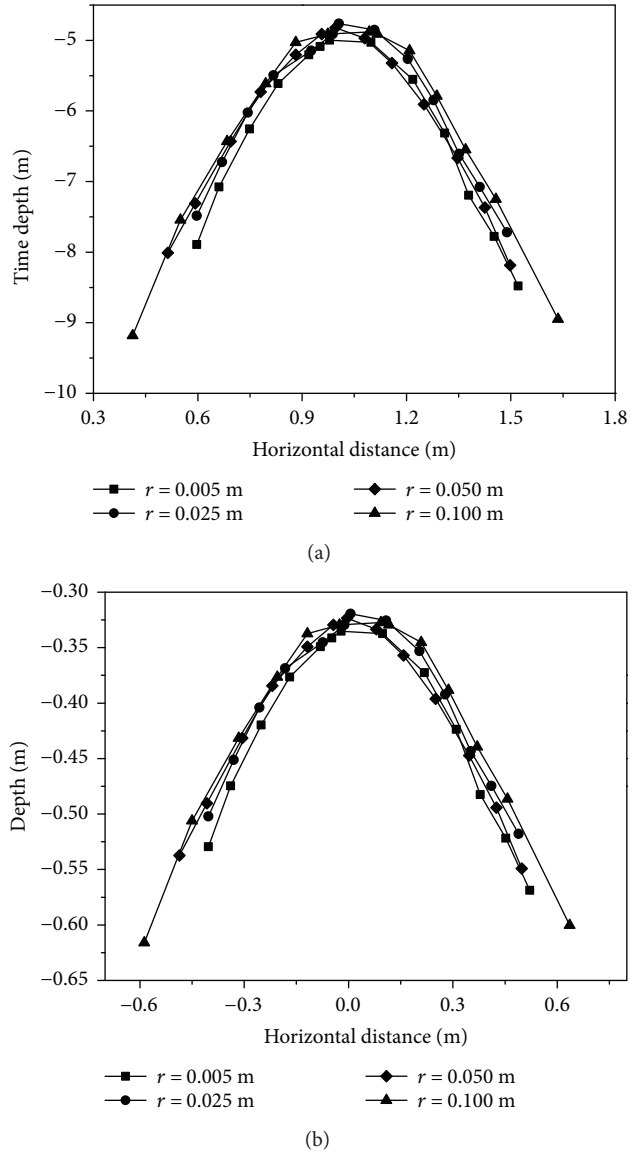


FIGURE 6: (a) Data conversion of time depth and distance in different object radius. (b) Data conversion of depth and distance in different object radius.

through the relationship between time depth and apparent depths (Formula S1). And then, the abscissa values of apparent depths were translated through horizontal axis

TABLE 1: Imaging feature of the object in different radius.

r/m	h/m	Long axis (a_r)	Short axis (b_r)	Hyperbolic formula
0.005	0.3	0.347	0.434	$\frac{y^2}{0.347^2} - \frac{x^2}{0.434^2} = 1$
0.025	0.3	0.333	0.388	$\frac{y^2}{0.333^2} - \frac{x^2}{0.388^2} = 1$
0.05	0.3	0.330	0.379	$\frac{y^2}{0.330^2} - \frac{x^2}{0.379^2} = 1$
0.100	0.3	0.342	0.408	$\frac{y^2}{0.342^2} - \frac{x^2}{0.408^2} = 1$

TABLE 2: Imaging feature of the object with different depth.

r/m	h/m	Long axis (a)	Short axis (b)	Hyperbolic formula
0.05	0.05	0.089	0.104	$\frac{y^2}{0.089^2} - \frac{x^2}{0.104^2} = 1$
0.05	0.10	0.133	0.159	$\frac{y^2}{0.133^2} - \frac{x^2}{0.159^2} = 1$
0.05	0.20	0.231	0.228	$\frac{y^2}{0.231^2} - \frac{x^2}{0.228^2} = 1$
0.05	0.30	0.330	0.379	$\frac{y^2}{0.330^2} - \frac{x^2}{0.379^2} = 1$
0.05	0.40	0.430	0.487	$\frac{y^2}{0.430^2} - \frac{x^2}{0.487^2} = 1$
0.05	0.50	0.531	0.598	$\frac{y^2}{0.531^2} - \frac{x^2}{0.598^2} = 1$
0.05	0.60	0.632	0.713	$\frac{y^2}{0.632^2} - \frac{x^2}{0.713^2} = 1$

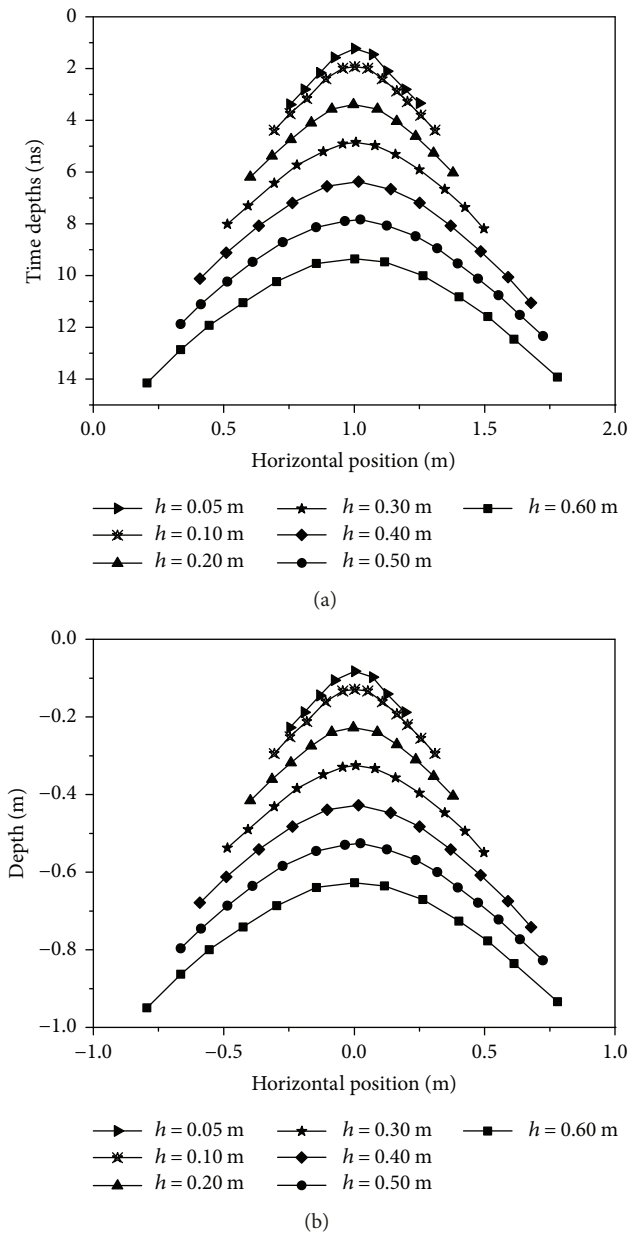


FIGURE 7: Data conversion of time depth and depth in different object depth.

in order that the abscissa values of peaks of hyperbolic curves reached zero (Table S2). So it is easy to fit the hyperbolic formulas. The imaging characteristics of time depths and apparent depths of different radius are shown in Figure 6.

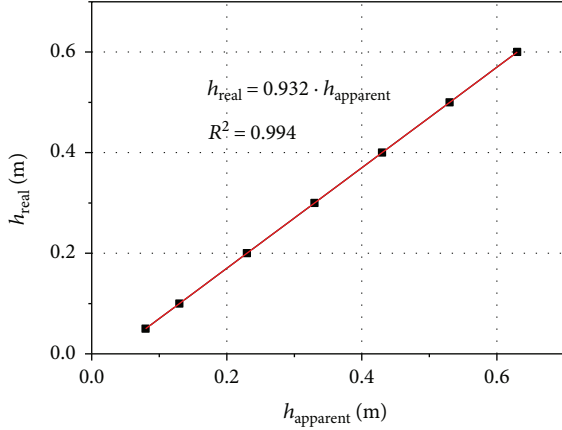
In Figure 6, the hyperbolic curves of depths of different radius are very close, and even some points are overlapped. It demonstrates that objects with different radius ($r=0.005\sim 0.100$ m) cannot be distinguished by imaging characteristics. In addition, the real depth of objects with different radius in the model is 0.30 m. However, the apparent depth of different radius is about 0.33 m. There is an error between apparent depth and real depth for the same radius, and it has been modified in Section 4.3.1.

The data of key points of hyperbolic curves are fitted by conjugate gradient method, and the hyperbolic formulas are obtained. The values of long and short axis are obtained by comparing hyperbolic formulas with (5). The detailed data are listed in Table 1. It can be seen that the values of long axis are changed from 0.330 to 0.347, when the object radius changed from 0.005 m to 0.100 m. And the values of short axis are changed from 0.379 to 0.434. In other words, the values of long and short axis are changed very small even though the radius changed 20 times. So the imaging characteristics do not show clear changes when the radius range is from 0.005 m to 0.100 m.

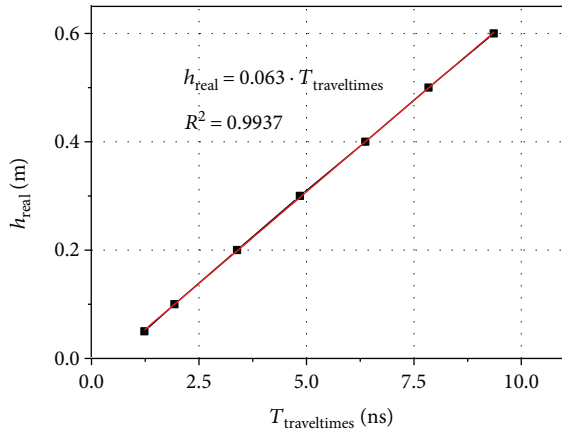
4.2. Imaging Characteristic Analysis of Objects with Different Depth. The method for extracting data is the same with that in Section 4.1. The coordinate values of time depths of different buried depth were obtained after manual sampling (Table S3). The coordinate values of apparent depths of different buried depth were obtained after depth transformation and coordinate translation (Table S4). The imaging characteristics of time depths and apparent depths of different buried depth are shown in Figure 7, when h is equal to 0.05 m, 0.10 m, 0.20 m, 0.30 m, 0.40 m, 0.50 m, and 0.60 m. In Figure 7, the hyperbolic curves of different buried depth are obviously changed. With the

TABLE 3: Comparison of the apparent depth and real depth with different depth.

Contents	Data						
Real depth h_{real}/m	0.05	0.10	0.20	0.30	0.40	0.50	0.60
Apparent depth $h_{\text{apparent}}/\text{m}$	0.08	0.13	0.23	0.33	0.43	0.53	0.63
Time depth $T_{\text{time}}/\text{ns}$	1.23	1.93	3.39	4.85	6.37	7.84	9.36



(a)



(b)

FIGURE 8: (a) Correction factor of real depths and apparent depths. (b) Correction factor of real depths and time depths.

increase of buried depths of objects, the depths of peaks of hyperbolic curves are increased. So the buried depths can be reflected by the depths of peaks of hyperbolic curves. In addition, the opening degree of hyperbola is increased with the buried depth increased.

The conjugate gradient method is also used to realize hyperbolic formula fitting. And the values of long and short axis hyperbolic formula are obtained by comparing hyperbolic formulas with (5). The detailed data are listed in Table 2. When the buried depths of objects changed from 0.05 m to 0.60 m, the values of long axis are changed from 0.089 to 0.632 (about 7 times). And the values of short axis are changed from 0.104 to 0.713 (about 7 times). In other words, both of the values of long and short axis are almost changed 7 times when the buried depths changed 0.55 m.

TABLE 4: Parameters of depth and radius of object, the long axis (a) and short axis (b).

t/ns	h/m	a_c^*	b_c^*	b_c/a_c	$(b_c/a_c)^*t$
1.23	0.05	0.08	0.10	1.24	0.76
1.93	0.10	0.12	0.15	1.25	1.21
3.39	0.20	0.21	0.26	1.22	2.07
4.85	0.30	0.31	0.37	1.22	2.96
6.37	0.40	0.40	0.48	1.21	3.85
7.84	0.50	0.49	0.60	1.21	4.74
9.36	0.60	0.59	0.71	1.20	5.64

* a_c and b_c represent the correction of long axis (a) and short axis (b) of hyperbolic curves, respectively.

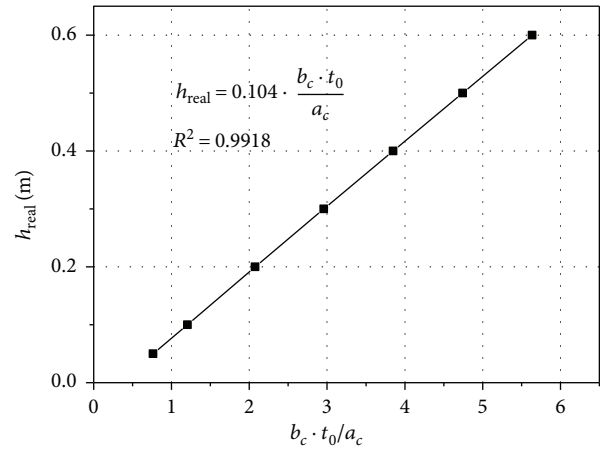


FIGURE 9: Correction factor of real depths and coefficient of the short and long axis.

So there are clear changes of imaging characteristics when the buried depths range is from 0.05 m to 0.60 m.

4.3. Inversion Model of Geometric Parameters and Long and Short Axis

4.3.1. Modified Model of Real Depth. In the forward imaging for FDTD method, there is an error between apparent depth and real depth. The main reason is that there are truncation errors between forward and backward differences of FDTD method. The value of truncation error is equal to the square of time-domain lattice (Δt). The real depths, apparent depths, and time depths of objects with different buried depths are listed in Table 3.

It can be seen that there are errors between real depths and apparent depths. Interestingly, the errors with different buried depths are the same, and are equal to 0.03 m. So

TABLE 5: Comparison of the real radius and inversion radius in different depth.

Contents	Data						
Real depth h_{real}/m	0.05	0.10	0.20	0.30	0.40	0.50	0.60
Real radius r_{real}/m	0.050	0.050	0.050	0.050	0.050	0.050	0.050
Inversion radius $r_{\text{inversion}}/\text{ns}$	0.089	0.065	0.054	0.051	0.049	0.049	0.047
Error e	78%	30%	8%	2%	2%	2%	6%

the errors can be modified and accurately real depth can be obtained.

$$h_{\text{real}} = 0.932 \cdot h_{\text{apparent}} \quad (10)$$

or

$$h_{\text{real}} = \frac{c}{\sqrt{\epsilon_r}} \cdot \frac{T}{2} = 0.063 \cdot T_{\text{traveltimes}} \quad (11)$$

Figure 8(a) is the fitting curve of real depth and apparent depth, and (10) is the modified relation between real depth and apparent depth. The depth error can be reduced using the modified relation. Figure 8(b) is the fitting curve of real depth and time depth, and (11) is the modified relation between real depth and time depth. The time depth of imaging can be quickly transformed into real depth using (11), and it is more valuable in application.

4.3.2. Inversion Model of Geometric Parameters and Long and Short Axis. The values of the long and short axis of hyperbolic imaging can be calculated by (8), (9), and the basic parameters of the forward model. Because the long and short axis of hyperbolic curves is not obviously affected by the change of radius, the imaging characteristics of objects are mainly affected by the change of buried depth. The long axis (a) and short axis (b) corresponding with real depth can be calculated by (11) and listed in Table 4.

According to (7) and (11), the relationship among real depth and long and short axis (a_c , b_c) of hyperbolic curves is fitted by binary fitting method. The correlation coefficient between real depth and axis is 0.104 from Figure 9; so the empirical (12) can be obtained.

$$h_{\text{real}} = 0.104 \cdot \frac{b_c \cdot t_0}{a_c} \quad (12)$$

The empirical (12) is a modified relation among real depth and long and short axis of hyperbolic curves. It can be seen that there is a difference between (12) and (7). And the difference is just reflected by the correction coefficient, which is equal to 0.104. Therefore, the accurate values of real depth can be quickly obtained by imaging characteristics of hyperbolic curves in practical application.

According to 12 and the data of Tables 3 and 4, the inversion model of object radius (13) can be obtained by nonlinear algorithm. The data of inversion radius and real radius of objects are listed in Table 5.

$$r_{\text{real}} = \frac{0.23}{h} \cdot \frac{b_c(a - (0.104/2) \cdot t_0)}{a_c} \quad (13)$$

TABLE 6: The antenna parameters of GPR.

Frequency	400 MHz
Emissivity	100 KHz
Ranges (ns)	40
Scanning speed (scan/s)	50
Gain	5

In Table 5, the errors of real radius and inversion radius are less than 8%, and inversion radius calculated by (13) is accurate when the depth range is from 0.20 m to 0.60 m. The corresponding errors of real depth of 0.05 m and 0.10 m are more than 30%. The reason is that there are big errors of fitting formulas of hyperbolic curves when the real depths are between 0.05 m and 0.10 m.

5. Inversion of the Measured GPR Data of the Heritage Building

5.1. Overview of the Heritage Building and Arrangement of Measuring Line. The heritage building built in 1384 during the early Ming Dynasty is a symbol of the city of Xi'an and one of the grandest of its kind in China. It covers an area of 1377 square meters and has 36 meters high and consisted of a foundation, a pedestal, and a tower. The structure of the tower is mainly made up of brick and wood and was built on the square base compacted by soil. At present, the pedestal shows some apparent fractures. It may be due to artificial disturbance and natural erosion, such as earthquake and subway.

GPR method is used to detect the internal deformations and distribution area in the pedestal. A distinct advantage of GPR is the ability to provide high-resolution continuous profiling for nondestructive site investigations. In addition, GPR has become economically feasible and convenient method in the protection of the heritage. Combining with the actual situation, antenna of 400 MHz frequency is an optimal choice because of the proper precision and detection depth. The detailed parameters of this antenna are listed in Table 6. Figure 10 shows the location of the heritage buildings, the leakage in the northeast of the pedestal, and monitoring survey area and the line layout. The survey lines are located in the northeast of the pedestal. Each line is 25 m length, and the distance between each line is 0.5 m.

After data processing and image interpretation, the results of GPR images show that abnormal regions of each survey line are distributed in the same location. So we use the data fragments of the abnormal regions to analyze the



FIGURE 10: (a–b) Location of the heritage buildings. (c) Leakage in external wall of the pedestal. (d) Monitoring survey area and the line layout.

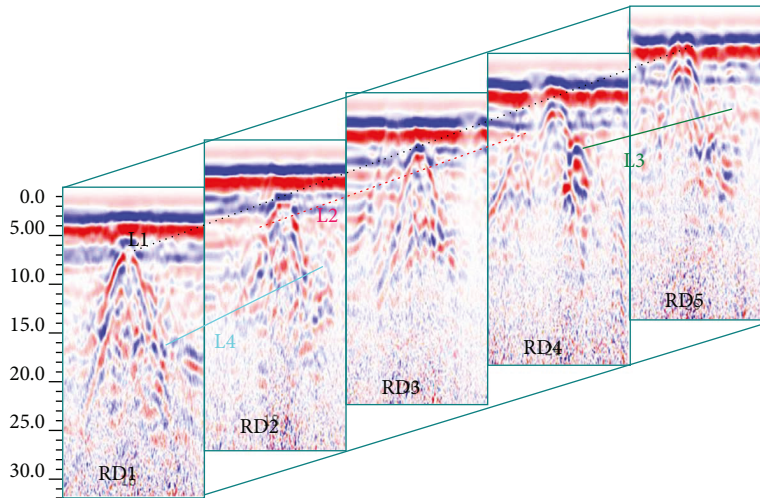


FIGURE 11: Geological section of anomaly region by GPR.

reasons of the complicated imaging. The length of each fragment is 1 m, and the slice figure consisted of the GPR images of each fragment in Figure 11.

In Figure 11, it can be obviously seen that there are typically hyperbolic reflection in the similar position of each line, and the depth of peaks of hyperbolic curves is about 0.4m. According to above results, the hyperbolic reflection can be deduced as point defects. The RD1 line is close to the main building, and the image of RD1 line

TABLE 7: Inversion parameters of depth and radius of the defects.

	<i>a</i>	<i>b</i>	<i>h/m</i>	<i>r/m</i>	<i>t/ns</i>
RD1 line	0.70	0.56	0.52	0.13	6.26
RD2 line	0.74	0.58	0.54	0.13	6.55
RD3 line	0.55	0.49	0.56	0.08	6.14
RD4 line	0.50	0.46	0.54	0.08	5.56
RD5 line	0.74	0.61	0.50	0.17	5.81

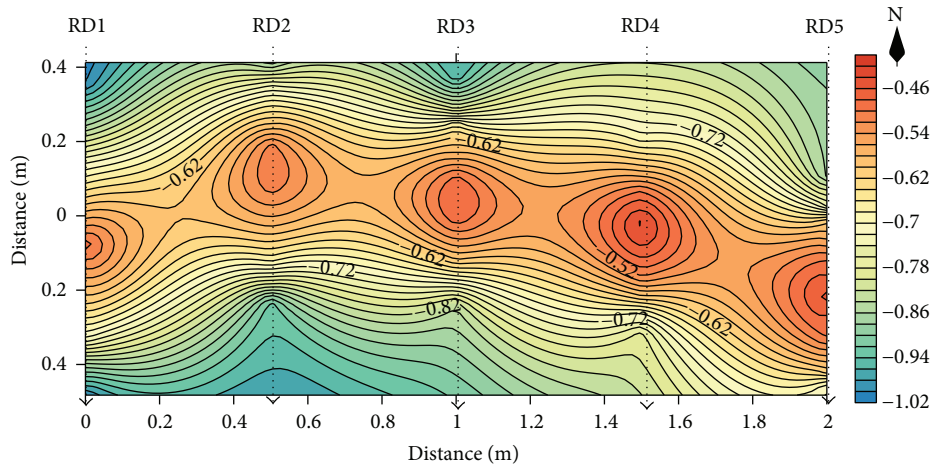


FIGURE 12: Inversion result of radius and depth of fracture.

has the strongest reflection. The reflection intensity of RD2, RD3, RD4, and RD5 lines is weakened change in order. This phenomenon reveals that the defects are consecutive and the geometry sizes of the defects are decreasing from RD1 to RD5 line. Through the contrast of the five GPR reflection images of the pedestal, it can deduce that the reflection characteristics of hyperbolic curves in the profile accord with penetrating fracture, which is marked as L1 line. Meanwhile, some filling materials (impurities or air) can be found nearby the main defects which are obtained from the GPR imaging, such as L2, L3, and L4 line.

5.2. Comprehensive Interpretation of Pedestal Defects of the Heritage Building. Feature points are extracted from the hyperbolic curves which have the strongest reflection intensity of each GPR images in Figure 11. And then the feature points are fitted to calculate the analytical equation of hyperbolic curves by conjugate gradient method. The depth and radius of objects in each GPR images could be estimated from the long axis and short axis of the hyperbolic curves. The detailed data are listed in Table 7.

In Table 7, the depth of the objects is 0.52 m, 0.54 m, 0.56 m, 0.54 m, and 0.50 m. The inversion depths are close to the seepage depths on the external wall (Figure 10(c)). The radius of the objects is 0.13 m, 0.13 m, 0.08 m, 0.08 m, and 0.08 m. The inversion radius is close to the width of the brick in the pedestal. So the falling bricks and the erosion of compacted soil are thought to be reasonable interpretation. On the basis of data interpolation and fitting, the initial values of depth and radius of L1 line are used to draw geological section map, which is shown in Figure 12.

In Figure 12, it can be visually observed that the five-point objects are connected to form a nonstraight penetrability fracture. The depth of the fracture is from 0.46 m to 0.60 m, and the width is about 0.15 m. The fracture reinforcement should be carried out, and the pedestal should be early protected with waterproof in case of monsoon.

6. Conclusions

In summary, we established the analytic relationship between depth and radius of object and long and short axis of hyperbolic equation, according to derivations of formulas.

$$\begin{aligned} r &= \frac{b(a-t_0)}{a}, \\ h_0 &= \frac{vt_0}{2} = \frac{bt_0}{a}. \end{aligned} \quad (14)$$

The image characteristics of hyperbolic curves with different depth and radius were studied by FDTD method. When $h = 0.3$ m, the intensity of reflected curves is obviously increased, with the increase of the radius from 0.005 m to 0.100 m but there is no obvious change of opening degree of hyperbolic curves. When $r = 0.05$ m, the depths of peaks of hyperbolic curves are increasing with the object depths increased from 0.05 m to 0.60 m, and the opening degrees of hyperbolic curves are gradually increased.

Inversion model of geometric parameters and long and short axis was established. The relationship among real depth and long and short axis (a_c , b_c) of hyperbolic curves was obtained.

$$h_{\text{real}} = 0.104 \cdot \frac{b_c \cdot t_0}{a_c}. \quad (15)$$

The inversion model of object radius was obtained by nonlinear algorithm.

$$r_{\text{real}} = \frac{0.23}{h} \cdot \frac{b_c(a - (0.104/2) \cdot t_0)}{a_c}. \quad (16)$$

The practical detection in heritage building was implemented according to the above research results, and its feasibility was verified. The detecting of pedestal defects of the heritage building is obviously effective by the inversion model. It is demonstrated that this inversion model is feasible, since the observed and calculated radius and depth of pedestal defects agree fairly well with each other.

Conflicts of Interest

The authors declare that they have no conflicts of interest.

Acknowledgments

The authors gratefully acknowledge the financial supports by China Postdoctoral Science Foundation (Grant no. 2017M613175), Shaanxi Province Science Foundation for youths (Grant no. 2018JQ5203) and Shaanxi Province Major Science Foundation (Grant no. 2018JZ5010). And the work was supported by the National Science Foundation of China (Grant no. 11572246, 51779207) and the Open Foundation of State Key Laboratory Base of Eco-Hydraulic Engineering in Arid Area (Grant no. 2016ZZKT-8).

Supplementary Materials

Formula S1: the equation of the object depth and two-way travel time. Figure S1: GETDATA obtains the key point coordinates by taking points continuously at the maximum amplitude of the reflection curve in GPR images. Table S1: data of the GPR imaging with different object radius. Table S2: transfer data of the GPR imaging with different object radius. Table S3: data of the GPR imaging with different object depth. Table S4: transfer data of the GPR imaging with different object depth. (*Supplementary Materials*)

References

- [1] J. L. Porsani, Y. B. Ruy, F. P. Ramos, and G. R. B. Yamanouth, "GPR applied to mapping utilities along the route of the line 4 (yellow) subway tunnel construction in São Paulo City, Brazil," *Journal of Applied Geophysics*, vol. 80, pp. 25–31, 2012.
- [2] S. Lahouar and I. L. Al-Qadi, "Automatic detection of multiple pavement layers from GPR data," *NDT & E International*, vol. 41, no. 2, pp. 69–81, 2008.
- [3] D. Breyse, "Nondestructive evaluation of concrete strength: an historical review and a new perspective by combining NDT methods," *Construction and Building Materials*, vol. 33, pp. 139–163, 2012.
- [4] S. K. U. Rehman, Z. Ibrahim, S. A. Memon, and M. Jameel, "Nondestructive test methods for concrete bridges: a review," *Construction and Building Materials*, vol. 107, pp. 58–86, 2016.
- [5] G. Lv, J. Yang, N. Li, D. Hu, Y. Zhang, and F. Zhao, "Dielectric characteristics of unsaturated loess and the safety detection of the road subgrade based on GPR," *Journal of Sensors*, vol. 2018, Article ID 5185460, 8 pages, 2018.
- [6] L. Lo Monte, D. Erricolo, F. Soldovieri, and M. C. Wicks, "Radio frequency tomography for tunnel detection," *IEEE Transactions on Geoscience and Remote Sensing*, vol. 48, no. 3, pp. 1128–1137, 2010.
- [7] E. Slob, "Interferometry by deconvolution of multicomponent multioffset GPR data," *IEEE Transactions on Geoscience and Remote Sensing*, vol. 47, no. 3, pp. 828–838, 2009.
- [8] E. Slob, M. Sato, and G. Olhoeft, "Surface and borehole ground-penetrating-radar developments," *Geophysics*, vol. 75, no. 5, pp. 75A103–75A120, 2010.
- [9] G. A. Meles, J. Van der Kruk, S. A. Greenhalgh, J. R. Ernst, H. Maurer, and A. G. Green, "A new vector waveform inversion algorithm for simultaneous updating of conductivity and permittivity parameters from combination crosshole/borehole-to-surface GPR data," *IEEE Transactions on Geoscience and Remote Sensing*, vol. 48, no. 9, pp. 3391–3407, 2010.
- [10] A. Di Matteo, E. Pettinelli, and E. Slob, "Early-time GPR signal attributes to estimate soil dielectric permittivity: a theoretical study," *IEEE Transactions on Geoscience and Remote Sensing*, vol. 51, no. 3, pp. 1643–1654, 2013.
- [11] A. P. Tran, M. R. M. Ardekani, and S. Lambot, "Coupling of dielectric mixing models with full-wave ground-penetrating radar signal inversion for sandy-soil-moisture estimation," *Geophysics*, vol. 77, no. 3, pp. H33–H44, 2012.
- [12] G. A. Meles, S. A. Greenhalgh, A. G. Green, H. Maurer, and J. van der Kruk, "GPR full-waveform sensitivity and resolution analysis using an FDTD adjoint method," *IEEE Transactions on Geoscience and Remote Sensing*, vol. 50, no. 5, pp. 1881–1896, 2012.
- [13] H. Chen and A. G. Cohn, "Probabilistic robust hyperbola mixture model for interpreting ground penetrating radar data," in *The 2010 International Joint Conference on Neural Networks (IJCNN)*, pp. 1–8, Barcelona, Spain, July 2010.
- [14] W. Al-Nuaimy, Y. Huang, M. Nakhkash, M. T. C. Fang, V. T. Nguyen, and A. Eriksen, "Automatic detection of buried utilities and solid objects with GPR using neural networks and pattern recognition," *Journal of Applied Geophysics*, vol. 43, no. 2–4, pp. 157–165, 2000.
- [15] C. Warren, A. Giannopoulos, and I. Giannakis, "gprMax: open source software to simulate electromagnetic wave propagation for ground penetrating radar," *Computer Physics Communications*, vol. 209, pp. 163–170, 2016.
- [16] I. Giannakis, A. Giannopoulos, and C. Warren, "A realistic FDTD numerical modeling framework of ground penetrating radar for landmine detection," *IEEE Journal of Selected Topics in Applied Earth Observations and Remote Sensing*, vol. 9, no. 1, pp. 37–51, 2016.



Hindawi

Submit your manuscripts at
www.hindawi.com

